PAPER

Check for updates

Hybrid films with excellent oxygen and water vapor barrier properties as efficient anticorrosive coatings†

Jiajie Wang, Ting Pan, Jian Zhang, Xiaozhi Xu, Qing Yin, Jingbin Han [iD] *
and Min Wei [iD]

Gas and moisture barrier materials are of crucial importance in various application fields, including food/drug packaging and encapsulation of electronic devices. Herein, a dual-barrier film to gas and water vapor was fabricated by a facile and cost-effective spin-coating of amphiphilic surfactant (Tween 80) modified LDH nanoplatelets (denoted as LDH-80) and polydimethylsiloxane (PDMS). The resultant (LDH-80/PDMS)$_{15}$ film exhibits low O_2 and H_2O transmission rates with ~0.701 and ~0.049 cm^3 m^{-2} d^{-1} atm^{-1}, respectively, smaller than those for most of the reported barrier materials. The remarkable barrier properties are ascribed to the prolonged diffusion length for gas permeation and improved inorganic–organic interfacial compatibility between LDH-80 and PDMS. Taking advantage of this unique dual-barrier property, an aluminum foil substrate coated with (LDH-80/PDMS)$_n$ film displays an excellent anti-corrosion effect due to the inhibition of oxygen-consuming corrosion, which enables the (LDH-80/PDMS)$_n$ films to be promising candidates in metal surface protection.

Introduction

Recently, flexible and transparent gas barrier films have evoked considerable attention in the encapsulation of electronic/photovoltaic devices and food/pharmaceutical packaging.[1–6] Organic–inorganic hybrid films have shown enhanced gas barrier properties rivaling pure polymer films,[7–12] while maintaining outstanding mechanical and optical properties.[13–19] However, a major drawback of these gas barrier composites is their sensitivity to humidity.[20,21] Under high humidity conditions, the gas barrier properties of these films decrease significantly due to the plasticization of polymer chains.[22,23] This phenomenon leads to an increase of gas permeability and thus limits their applicability. Furthermore, the infiltrating water molecules would interact with metals or germs, which results in metal corrosion or decrease in food shelf-life. Therefore, how to fabricate composite films that can block gas and moisture simultaneously remains a big challenge.

As one type of important two dimensional (2D) inorganic materials, layered double hydroxides (LDHs) have been extensively applied for the preparation of organic–inorganic hybrid materials, and have shown potential applications in

drug delivery, energy storage and smart response.[24–31] Our recent work reported the design and assembly of LDH/polymer films as effective barrier materials toward O_2, N_2, CO_2 and He gas.[32–35] Their barrier property is ascribed to the prolonged diffusion pathway of gas molecules with the introduction of LDH nanosheets, and the decreased free volume by the modification of organic–inorganic interface. However, upon long-term exposure in moisture atmosphere, their gas barrier property will be damaged. The hydrophilic characteristic of LDHs and polymers enables the adsorption/diffusion of water molecule into films, resulting in the plasticization of polymer matrix and finally deterioration of the gas barrier property. To solve this problem, a dual-barrier film toward gas and water vapor by assembling surfactant-modified LDH with a hydrophobic polymer would be a promising candidate.

In this work, an organic–inorganic composite film was fabricated *via* alternate spin-coating technique, consisting of an amphiphilic surfactant (Tween 80) modified LDH nanoplatelets (denoted as LDH-80) and polydimethylsiloxane (PDMS) as building blocks (Scheme 1). The resulting (LDH-80/PDMS)$_n$ films show dual-barrier behavior toward water and oxygen molecule simultaneously. The combination of oxygen and water dual-barrier performance in one single film has rarely been demonstrated in previous reports. By virtue of such an interesting property, the aluminum foil coated by (LDH-80/PDMS)$_n$ film exhibits a suppressed oxygen-consuming corrosion in an oxygen/moisture enriched atmosphere.

State Key Laboratory of Chemical Resource Engineering, Beijing Advanced Innovation Center for Soft Matter Science and Engineering, Beijing University of Chemical Technology, Beijing, 100029, China. E-mail: hanjb@mail.buct.edu.cn; Tel: +86-10-64412131
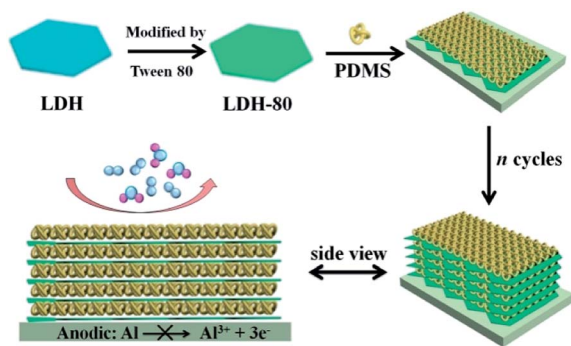
Scheme 1 Schematic illustration for the assembly process of (LDH-80/PDMS)$_n$ film on aluminum foil substrate for anti-corrosion protection.

Experimental

Reagents and materials

Analytical grade chemicals including Mg(NO$_3$)$_2$·6H$_2$O, Al(NO$_3$)$_3$·9H$_2$O, NaOH, concentrated sulphuric acid (H$_2$SO$_4$), hydrogen peroxide (H$_2$O$_2$) and polydimethylsiloxane (PDMS) were obtained from Beijing Yili Fine Chemicals Co. Ltd. Tween 80 (Fig. S1, ESI†) was purchased from Aladdin Chemicals Co. Ltd. and used without further purification. Deionized water was used in all the experiments.

Synthesis of MgAl-LDH colloid

MgAl-LDH colloid was synthesized by the separate nucleation and aging steps method reported by our group.[36,37] Typically, 100 ml mixed salt solution (Mg(NO$_3$)$_2$·6H$_2$O: 0.2 M and Al(NO$_3$)$_3$·9H$_2$O: 0.1 M) and 400 ml NaOH solution (0.15 M) were simultaneously added to a colloid mill with rotor speed of 3000 rpm and mixed for 1 min. The resulting slurry was obtained *via* centrifugation and washed several times and then dispersed in 400 ml of deionized water. This aqueous suspension was transferred into a stainless steel autoclave with a Teflon lining. Upon hydrothermal treatment at 110 °C for 24 h, the LDH colloidal suspension was obtained after removal of the precipitate.

Modification of LDH by Tween 80

Tween 80 (5 ml) was added to 200 ml LDH colloidal suspension (solid content: 1.14%), followed by stirring vigorously for 4 h at room temperature. After that, the LDH nanoplatelet was modified by Tween 80 (defined as LDH-80). Subsequently, the modified LDH was washed thoroughly with water to remove the excess Tween 80. Finally, the LDH-80 was dispersion in water to form a stable colloidal suspension (solid content: ~1.0%) to fabricate (LDH-80/PDMS)$_n$ films.

Fabrication of the (LDH-80/PDMS)$_n$ films

The (LDH-80/PDMS)$_n$ films were constructed on specific substrates by applying the spin-coating technique. Polyethylene terephthalate (PET) film was used as substrate for oxygen/water vapor transmission rate test; Al foil was employed for the measurement of

anticorrosive property; and quartz glass substrate (purity > 99.9%) was used for other characterizations. Prior to deposition, the substrates were treated in an ultrasonic bath with deionized water, ethanol and acetone for 10 min sequentially. PDMS was selected due to its hydrophobic characteristic and excellent film-forming property. The LDH-80 colloidal suspension (~1%) and pure PDMS liquid without solvent were spin-coated onto a pre-cleaned substrate with 2000 rpm for 60 s and 5000 rpm for 60 s alternately. The film was dried at ambient temperature in air for 20 min after each spin-coating process. Subsequently, a series of these operations for LDH-80 and PDMS were repeated *n* times to obtain the (LDH-80/PDMS)$_n$ multilayer films. The initial and terminational layers are LDH-80 and PDMS, respectively. As a comparison sample, the (LDH/PDMS)$_n$ films using unmodified LDH were prepared by a similar spin-coating process.

Results and discussion

Characterization of LDH and LDH-80

Fig. 1A illustrates the XRD pattern of the MgAl-LDH sample with 2θ at 10.2°, 20.3°, 34.9°, 38.1° and 61.0°, which can be indexed as (003), (006), (012), (015) and (110) reflections of a nitrate-LDH phase. No other crystalline phase is detected, indicating the high purity of the product. SEM image of the LDH shows hexagonal plate-like nanocrystals with diameter of ~105 nm (Fig. 1B). The LDH nanoplatelets were then modified with an amphipathic surfactant (Tween 80) to construct a hydrophobic surface (denoted as LDH-80) for the enhancement of interfacial compatibility with polymer. The XRD pattern of LDH-80 shows a (003) diffraction in the same position as that of pristine LDH, which illustrates the interlayer spacing of LDH keeps unchanged, indicting the absence of Tween 80 in LDH interlayer. Fig. 1D illustrates LDH-80 nanoplatelets maintain its original plate-like morphology, with a particle size distribution of 75–152 nm and an average size of ~110 nm (Fig. S2, ESI†). In addition, the weight loading of Tween 80 in the LDH-80 hybrid was calculated to be 12.5% from thermogravimetric analysis (TGA, Fig. S3, ESI†).

The modification of LDH with Tween 80 was further illustrated by FT-IR spectra. The characteristic FT-IR bands of Tween 80 are assigned as follows (Fig. 2, red curve): 3550 cm^{-1} (–OH stretching vibration), 2927 cm^{-1} (–CH stretching of –CH$_3$ groups), 2852 cm^{-1} (–CH stretching of –CH$_2$ groups), 1740 cm^{-1} (C=O stretching) and 1095 cm^{-1} (C–O–C bonding). For LDH (black curve), the bands at 3480 and 1630 cm^{-1} are attributed to the hydroxy (–OH) stretching vibration of its host layer and interlayer crystal water, respectively. Bands at 1380 and 740 cm^{-1} indicate the presence of NO$_3^-$ in LDH gallery. In the case of LDH-80 sample (blue curve), the characteristic peaks of both LDH and Tween 80 are observed. It should be noted that the band of C=O stretching vibration for LDH-80 shows a red-shift relative to Tween-80 (from 1740 cm^{-1} to 1660 cm^{-1}). In contrast, this band remains unchanged (1740 cm^{-1}) for the physical mixture of LDH and Tween 80, the C=O stretching vibration appears at 1740 cm^{-1} (Fig. S4, ESI†). These results may suggest the presence of interfacial interaction between Tween 80 and LDH.
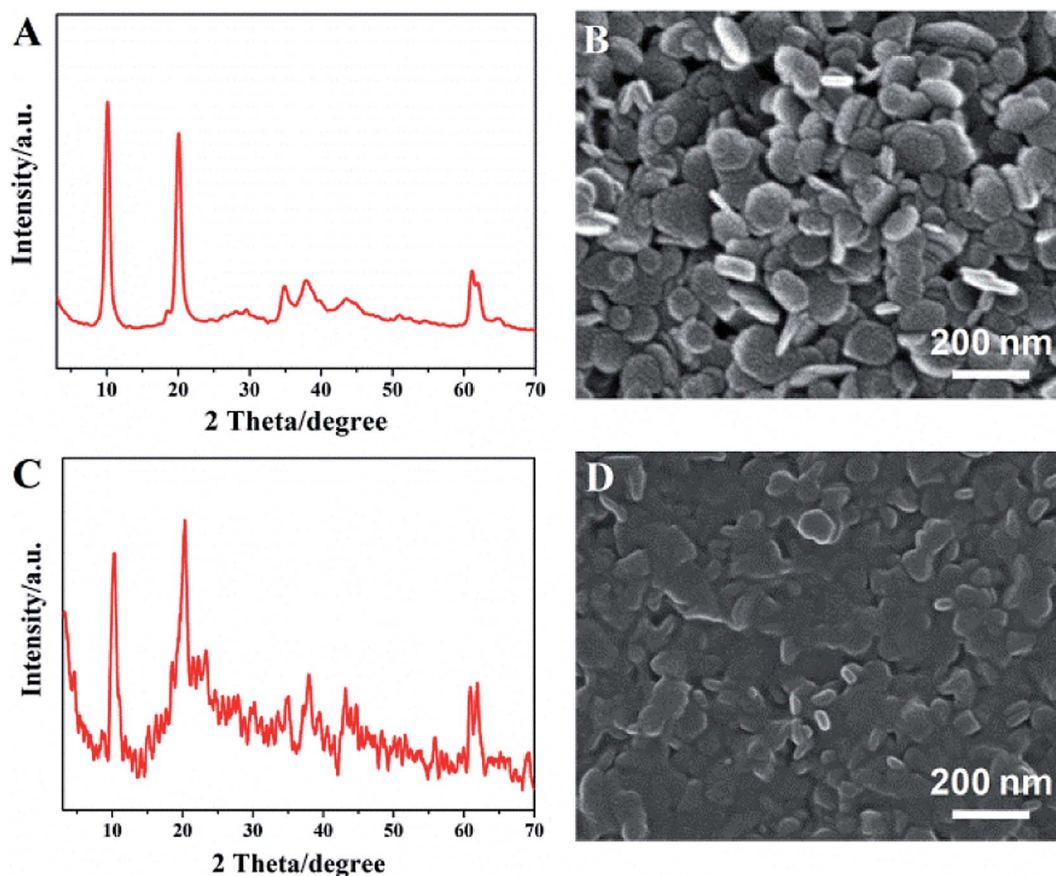
Fig. 1 XRD patterns and SEM images of pristine LDH (A and B) and Tween 80 modified LDH (C and D).

Structural and morphological analyses of (LDH-80/PDMS)$_n$ films

UV-vis absorption spectra of the (LDH-80/PDMS)$_n$ films with various bilayer numbers are shown in Fig. 3A. The characteristic absorption intensity of PDMS at 192 nm enhances linearly with the increase of bilayer number n (Fig. 3A, inset), indicating a stepwise and regular growth process for the (LDH-80/PDMS)$_n$

Fig. 2 FT-IR spectra of Tween 80, pristine LDH and LDH-80 samples.

films. XRD pattern (Fig. S5, ESI†) of the obtained (LDH-80/PDMS)$_{15}$ film displays a peak at $2\theta = 10.2°$, which is attributed to the (003) reflection of the LDH phase.

The top-view SEM image (Fig. 3B) displays the homogeneity of the (LDH-80/PDMS)$_{15}$ film. The thickness of (LDH-80/PDMS)$_n$ films with various n can be estimated from their side-view SEM images (inset of Fig. 3B and S6, ESI†), which increases gradually from 3.47 to 12.95 μm as the bilayer number varies from 3 to 15, indicating an average thickness increment of 0.89 μm per bilayer cycle (Fig. S7, ESI†). Upon scratching of the film surface, no delamination or peeling occurs, demonstrating a strong adhesion of the film to the substrate (Fig. S8, ESI†). The AFM topographical image (5 μm × 5 μm) of the (LDH-80/PDMS)$_{15}$ film along with a respective surface profile is illustrated in Fig. S9 (ESI†), from which a homogeneous and smooth surface is observed with root mean square roughness (R_q) of ~10.9 nm. In comparison, the R_q value for (LDH/PDMS)$_n$ and pure PDMS film is ~37.6 and ~7.2 nm, respectively (Fig. S10, ESI†). The relatively higher surface roughness of (LDH/PDMS)$_n$ film is probably related with its lower interfacial compatibility between LDH and PDMS. In addition, the (LDH/PDMS)$_{15}$ film shows a remarkable optical transparency (Fig. S11, ESI†) with an average transmittance of ~76% in 400–800 nm.

The arrangement of inorganic lamella is one of the crucial parameters governing the barrier property of organic–inorganic films. The orientation of LDH platelets in (LDH-80/PDMS)$_n$
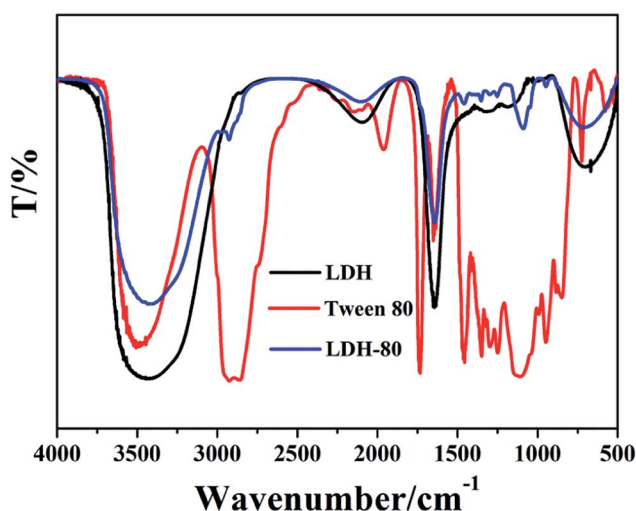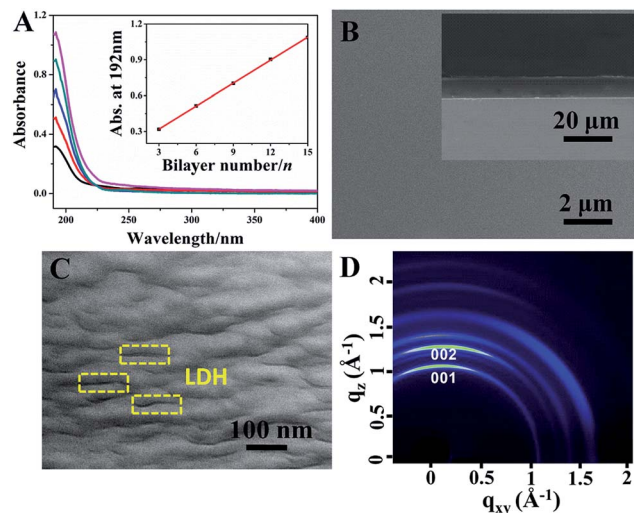
Fig. 3 (A) UV-vis absorption spectra of the (LDH-80/PDMS)$_n$ (n = 3–15) films on quartz glass substrates (inset: the linear relationship between absorbance at 192 nm and bilayer number n); (B) top-view and side-view (inset) SEM images of (LDH-80/PDMS)$_{15}$ film; (C) side-view TEM image and (D) 2D grazing-incidence XRD patterns for (LDH-80/PDMS)$_{15}$ film.

films was observed by TEM using a resin-embedding and section method (see details in the ESI†), which shows the layers of LDH platelets as some dark lines with a distinct stratified architecture (Fig. 3C), illustrating the good dispersion and high orientation of LDH platelets in the hybrid films. In addition, the 2D grazing-incidence XRD pattern of the (LDH-80/PDMS)$_{15}$ film displays increased reflections along the q_{xy} (in-plane) axes (Fig. 3D), further indicating the parallel orientation of LDH platelets to the substrate.

The surface wettability of a film is closely related with its water molecule permeation property. The water contact angle test was performed to investigate the surface wettability of resultant films. As shown in Fig. 4, the bare substrate, LDH and (LDH/PDMS)$_{15}$ (fabricated by using unmodified LDH) film are hydrophilic with water contact angle less than 90°. The pure PDMS film shows a slightly hydrophobic feature with water contact angle of 97°. In contrast, the (LDH-80/PDMS)$_{15}$ film exhibits a water contact angle of 115°, indicative of a more
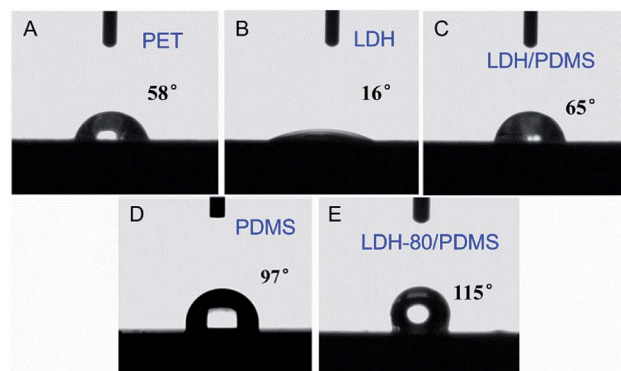
hydrophobic surface. The hydrophobic surface of (LDH-80/PDMS)$_{15}$ coating would facilitate the improvement of water vapor barrier property.

Oxygen/water vapor dual-barrier performance of (LDH-80/PDMS)$_n$ films

The oxygen transmission rate (OTR) and water vapor transmission rate (WVTR) were measured to investigate the barrier property of (LDH-80/PDMS)$_n$ films on PET substrate (Fig. 5). The pristine PET film displays OTR and WVTR of ~111.271 and ~31.788 cm^3 m^{-2} d^{-1} atm^{-1}, respectively. The coating of (LDH-80/PDMS)$_n$ films leads to dramatic decrease in OTR and WVTR. It is observed that the OTR values for (LDH-80/PDMS)$_n$ films reduce from ~68.589 to ~0.701 cm^3 m^{-2} d^{-1} atm^{-1}; and the WVTR values decrease from ~12.153 to ~0.049 cm^3 m^{-2} d^{-1} atm^{-1} as the bilayer number n increases from 5 to 15. In contrast, the pure PDMS film with the same thickness as (LDH-80/PDMS)$_{15}$ film displays a relatively weak barrier ability with OTR of ~106.032 cm^3 m^{-2} d^{-1} atm^{-1} and an unexceptional reduction of WVTR to ~18.492 cm^3 m^{-2} d^{-1} atm^{-1} (Fig. S12, ESI†). In addition, the (LDH/PDMS)$_{15}$ film exhibits higher OTR and WVTR values compared with (LDH-80/PDMS)$_{15}$ film, which is ascribed to the weak interfacial compatibility between LDH and PDMS matrix. The results illustrate the incorporation of highly-oriented LDH-80 nanoplates suppresses the diffusion of O$_2$ and H$_2$O molecules as a result of the increased diffusion length; the hydrophobicity of the (LDH-80/PDMS)$_{15}$ film further prohibits the adsorption of water molecule to the film surface and hence an enhanced water vapor barrier property is achieved. Compared with other reported barrier materials, the oxygen and water vapor barrier properties of (LDH-80/PDMS)$_{15}$ films is among the highest level (Table S1, ESI†). And the dual-barrier performance of (LDH-80/PDMS)$_{15}$ film would be sufficient for food packaging and encapsulation of electronic devices, such as LCD/LED display and photovoltaic module (Fig. S13, ESI†).

The anti-corrosion property of (LDH-80/PDMS)$_n$ films

Base on the unique dual-barrier property of the (LDH-80/PDMS)$_n$ films toward oxygen and water vapor, it is expected that
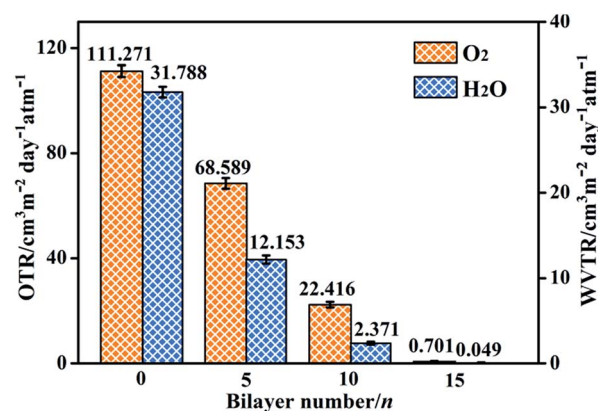

Fig. 4 Water contact angle measurements on (A) bare PET, (B) pristine LDH, (C) (LDH/PDMS)$_{15}$, (D) pure PDMS and (E) (LDH-80/PDMS)$_{15}$ film.

Fig. 5 OTR and WVTR values of bare PET substrate (n = 0) and (LDH-80/PDMS)$_n$ films with n = 5, 10 and 15, respectively.

such films may impose anti-corrosion effect on the metal protection, as the metallic corrosion is induced by the oxidation under oxygen and moisture-enriched conditions. The (LDH-80/PDMS)$_n$ films were assembled on Al foil substrate to study the anti-corrosion effect by examining their electrochemical impedance spectroscopy (EIS) and polarization curves in 3.5 wt% NaCl aqueous solution. The Nyquist plots of (LDH-80/PDMS)n films are presented in Fig. 6A. It is observed that the (LDH-80/PDMS)$_n$ films exhibit an increment in the order of magnitudes for interfacial electron-transfer resistance upon increasing bilayer number from 5 to 15, indicating an improved anti-corrosion behavior. Moreover, compared with the bare Al substrate, PDMS and (LDH/PDMS)$_{15}$ films, the (LDH-80/PDMS)$_{15}$ film displays the largest electron-transfer resistance (Fig. 6B), indicative of the best anti-corrosion property, which is ascribed to its superior oxygen and water molecule barrier behavior.

Tafel extrapolation measurements (Fig. 7A) were carried out to give a further understanding on the metallic protection by (LDH-80/PDMS)$_n$ films. The bare Al substrate shows a corrosion potential (E_{corr}) of -1418 mV; while the E_{corr} of (LDH-80/PDMS)$_n$ coated Al exhibits a positive shift from -1276 to -672 mV as n increases from 5 to 15. The corrosive current density (I_{corr}) of the (LDH-80/PDMS)$_{15}$ film decreases by more than 3 orders of magnitude compared with that of untreated Al substrate. In

Fig. 7 (A) Potentiodynamic polarization curves of bare Al substrate, (LDH-80/PDMS)$_n$ films on Al substrate with n = 5, 10 and 15; (B) Potentiodynamic polarization curves of PDMS, (LDH/PDMS)$_{15}$ and (LDH-80/PDMS)$_{15}$ film, respectively.

addition, the (LDH-80/PDMS)$_{15}$ film shows a larger E_{corr} and smaller I_{corr}, in comparison with pure PDMS and (LDH/PDMS)$_{15}$ film (Fig. 7B), indicating its better anti-corrosion effect. The Tafel extrapolation test combined with EIS measurement demonstrate that the dual-barrier property of (LDH-80/PDMS)$_{15}$ film exerts a remarkable anti-corrosion performance toward the metal surface protection.

In addition, the anti-corrosion effect of (LDH-80/PDMS)$_{15}$ film on Al substrates was further confirmed by SEM. The bare Al foil exhibits a uniform surface without any corrosion (Fig. 8A);
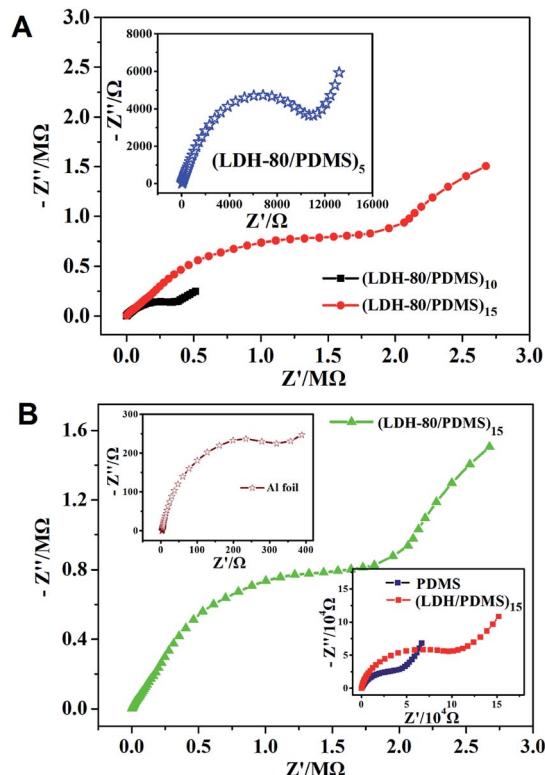

Fig. 6 (A) Nyquist plots of the impedance for (LDH-80/PDMS)$_n$ films on Al substrate with n = 5 (inset), 10 and 15; (B) Nyquist plots of the impedance for various samples, including (LDH-80/PDMS)$_{15}$ film, bare Al substrate (top left), PDMS and (LDH/PDMS)$_{15}$ film (bottom right). The red line in A is the same as the green line in B for giving a clear comparison.
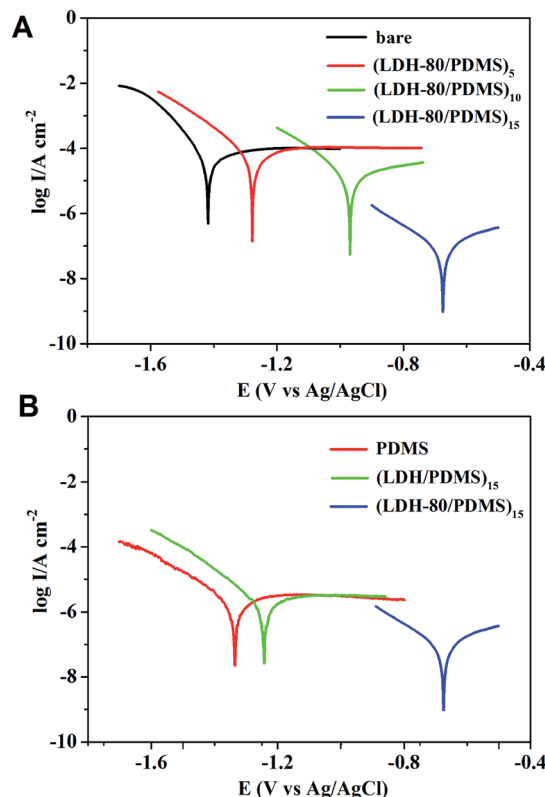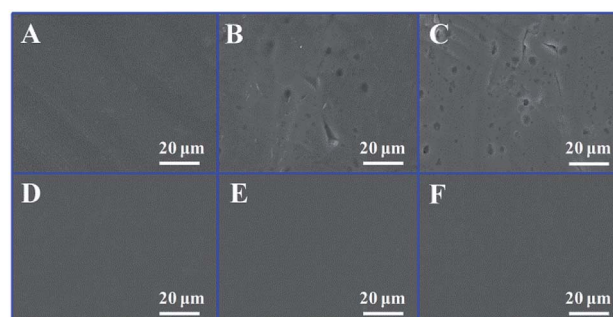

Fig. 8 Top-view SEM images of Al substrate dipping into a 3.5% NaCl solution for (A) 0 day, (B) 90 days and (C) 180 days, respectively; top-view SEM images of (LDH-80/PDMS)$_{15}$ film coated Al substrate dipping into the same solution for (D) 0 day, (E) 90 days and (F) 180 days, respectively.

after dipping into a 3.5% NaCl solution in air for 90 days, an obvious pitting corrosion was observed on the surface (Fig. 8B); this became more serious with an extension to 180 days (Fig. 8C). In contrast, the $(LDH-80/PDMS)_{15}$ film coated Al substrate did not undergo obvious corrosion at the same conditions (Fig. 8D–F). The results demonstrate the potential application of $(LDH-80/PDMS)_n$ films in the protection of metal surface.

Conclusions

In summary, organic–inorganic $(LDH-80/PDMS)_n$ films are fabricated by an alternate spin-coating method, which display excellent oxygen and water vapor dual-barrier property. The enhanced O_2 gas barrier property is mainly due to the elongation of diffusion path; while the water vapor barrier behavior is attributed to the synergistic effect of hydrophobicity and increased diffusion path. By virtue of such dual-barrier property, the Al substrate coated by $(LDH-80/PDMS)_n$ films shows a significantly improved anti-corrosion effect through restraining the oxygen-consuming corrosion. Therefore, this work provides a new strategy for developing oxygen/water vapor dual-barrier films, which are highly needed for a variety of applications, including metal anti-corrosion, food/pharmaceutical packaging and electronics encapsulation.

Conflicts of interest

There are no conflicts to declare.

Acknowledgements

Notes and references

1 Y. Yang, L. Bolling, M. Haile and J. C. Grunlan, *RSC Adv.*, 2012, **2**, 12355–12363.

2 N. Yan, F. Capezzuto, M. Lavorgna, G. G. Buonocore, F. Tescione, H. Xia and L. Ambrosio, *Nanoscale*, 2016, **8**, 10783–10791.

3 T. Kim, J. H. Kang, S. J. Yang, S. J. Sung, Y. S. Kim and C. R. Park, *Energy Environ. Sci.*, 2014, **7**, 3403–3411.

4 M. Wang, V. Janouta and S. L. Regen, *Chem. Commun.*, 2013, **49**, 3576–3578.

5 S. Seethamraju, P. C. Ramamurthy and G. Madras, *RSC Adv.*, 2014, **4**, 11176–11187.

6 J. Yoo, S. B. Lee, C. K. Lee, S. W. Hwang, C. Kim, T. Fujigaya, N. Nakashima and J. K. Shim, *Nanoscale*, 2014, **6**, 10824–10830.

7 A. Mace, K. Laasonenb and A. Laaksonen, *Phys. Chem. Chem. Phys.*, 2014, **16**, 166–172.

8 C. Xiang, P. J. Cox, A. Kukovecz, B. Genorio, D. P. Hashim, Z. Yan, Z. Peng, C.-C. Hwang, G. Ruan, E. G. Samuel, P. M. Sudeep, Z. Konya, R. Vajtai, P. M. Ajayan and J. M. Tour, *ACS Nano*, 2013, **7**, 10380–10386.

9 S. Cheng, Y. Zhang, R. Cha, J. Yang and X. Jiang, *Nanoscale*, 2016, **8**, 973–978.

10 Y. Lin, Z. Zeng, J. Zhu, S. Chen, X. Yu and L. Liu, *RSC Adv.*, 2015, **5**, 57771–57780.

11 Y.-H. Yang, L. Bolling, M. A. Priolo and J. C. Grunlan, *Adv. Mater.*, 2013, **25**, 503–508.

12 C. Zhang, C. Zhang, R. Ding, X. Cui, J. Wang, Q. Zhang and Y. Xu, *ACS Appl. Mater. Interfaces*, 2016, **8**, 14766–14775.

13 Y. C. Li, J. Schulz, S. Mannen, C. Delhom, B. Condon, S. Chang, M. Zammarano and J. C. Grunlan, *ACS Nano*, 2010, **4**, 3325–3337.

14 A. J. Svagan, A. Åkesson, M. Cárdenas, S. Bulut, J. C. Knudsen, J. Risbo and D. Plackett, *Biomacromolecules*, 2012, **13**, 397–405.

15 H. Liu, T. Kuila, N. H. Kim, B. C. Ku and J. H. Lee, *J. Mater. Chem. A*, 2013, **1**, 3739–3746.

16 S. Zhou, J. Chen, X. Li, X. Ji, G. Zhong and Z. Li, *RSC Adv.*, 2016, **6**, 2530–2536.

17 M. A. Priolo, D. Gamboa, K. M. Holder and J. C. Grunlan, *Nano Lett.*, 2010, **10**, 4970–4974.

18 H. Huang, C. Liu, D. Li, Y. Chen, G. Zhong and Z. Li, *J. Mater. Chem. A*, 2014, **2**, 15853–15863.

19 C. Aulin, G. S. Alvarez and T. Lindström, *Nanoscale*, 2012, **4**, 6622–6628.

20 S. Burgess, J. Lee, C. Mubarak, R. Kriegel and W. Koros, *Polymer*, 2015, **65**, 34–44.

21 Y. Wang, Q. Yang, J. Li, J. Yang and C. Zhong, *Phys. Chem. Chem. Phys.*, 2016, **18**, 8352–8358.

22 K. Bhunia, H. Zhang, F. Liu, B. Rasco, J. Tanga and S. Sablani, *Innovative Food Sci. Emerging Technol.*, 2016, **38**, 124–130.

23 S. Despond, E. Espuche and A. Domard, *J. Polym. Sci., Part B: Polym. Phys.*, 2001, **39**, 3114–3127.

24 L. Wu, Z. Hu, G. Chen and Z. Li, *Soft Matter*, 2015, **11**, 9038–9044.

25 Y. Wang, D. Zhang, Q. Bao, J. Wu and Y. Wan, *J. Mater. Chem.*, 2012, **22**, 23106–23113.

26 G. Abellán, E. Coronado, C. Martí-Gastaldo, A. Ribera, J. L. Jordá and H. García, *Adv. Mater.*, 2014, **26**, 4156–4162.

27 Z. Gu, J. J. Atherton and Z. P. Xu, *Chem. Commun.*, 2015, **51**, 3024–3036.

28 W. Shi, Y. Jia, S. Xu, Z. Li, Y. Fu, M. Wei and S. Shi, *Langmuir*, 2014, **30**, 12916–12922.

29 L. Yan, W. Chen, X. Zhu, L. Huang, Z. Wang, G. Zhu, V. A. L. Roy, K. N. Yu and X. Chen, *Chem. Commun.*, 2013, **49**, 10938–10940.

30 S. Sene, S. Bégu, C. Gervais, G. Renaudin, A. Mesbah, M. E. Smith, P. H. Mutin, A. van der Lee, J.-M. Nedelec, C. Bonhomme and D. Laurencin, *Chem. Mater.*, 2015, **27**, 1242–1254.

31 T. Tsai, B. Naveen, W. Shiu and S. Lu, *RSC Adv.*, 2014, **4**, 25683–25691.

32 Y. Dou, S. Xu, X. Liu, J. Han, H. Yan, M. Wei, D. G. Evans and X. Duan, *Adv. Funct. Mater.*, 2014, **24**, 514–521.

33 Y. Dou, T. Pan, S. Xu, H. Yan, J. Han, M. Wei, D. G. Evans and X. Duan, *Angew. Chem., Int. Ed.*, 2015, **54**, 9673–9678.

34 T. Pan, S. Xu, Y. Dou, X. Liu, Z. Li, J. Han, H. Yan and M. Wei, *J. Mater. Chem. A*, 2015, **3**, 12350–12356.

35 Y. Dou, A. Zhou, T. Pan, J. Han, M. Wei, D. Evans and X. Duan, *Chem. Commun.*, 2014, **50**, 7136–7138.

36 J. Han, Y. Dou, M. Wei, D. G. Evans and X. Duan, *Angew. Chem., Int. Ed.*, 2010, **49**, 2171–2174.

37 Y. Dou, J. Han, T. Wang, M. Wei, D. G. Evans and X. Duan, *Langmuir*, 2012, **28**, 9535–9542.